mathematics

MDPI

Article

Vehicle Response to Kinematic Excitation, Numerical Simulation Versus Experiment

Jozef Melcer [1], Eva Merčiaková [1], Mária Kúdelčíková [1] and Veronika Valašková [1,*]

[1] Department of Structural Mechanics and Applied Mathematics, Faculty of Civil Engineering, University of Zilina, 01009 Zilina, Slovakia; jozef.melcer@uniza.sk (J.M.); eva.merciakova@uniza.sk (E.M.); maria.kudelcikova@uniza.sk (M.K.)

* Correspondence: veronika.valaskova@uniza.sk; Tel.: +421-41-513-5606

Abstract: The article is devoted to the numerical simulation and experimental verification of a vehicle's response to kinematic excitation caused by driving along an asphalt road. The source of kinematic excitation was road unevenness, which was mapped by geodetic methods. Vertical unevenness was measured in 0.25 m increments in two longitudinal profiles of the road spaced two meters apart with precise leveling realized by geodetic digital levels. A space multi-body computational model of a Tatra 815 heavy truck was adopted. The model had 15 degrees of freedom. Nine degrees of freedom were tangible and six degrees of freedom were intangible. The equations of motion were derived in the form of second-order ordinary differential equations and were solved numerically by the Runge–Kutta method. A custom computer program in MATLAB was created for numerical simulation of vehicle movement (eps = 2^{-52}). The program allowed simulation of quantities such as deflections, speeds, accelerations at characteristic points of the vehicle, and static or dynamic components of contact forces arising between the wheel and the road. The response of the vehicle (acceleration at characteristic points) at different speeds was experimentally tested. The experiment was numerically simulated and the results were mutually compared. The basic statistical characteristics of experimentally obtained and numerically simulated signals and their power spectral densities were compared.

Keywords: numerical simulation; experimental test; heavy truck; kinematic quantities; statistical characteristics

Citation: Melcer, J.; Merčiaková, E.; Kúdelčíková, M.; Valašková, V. Vehicle Response to Kinematic Excitation, Numerical Simulation Versus Experiment. *Mathematics* **2021**, *9*, 678. https://doi.org/10.3390/math9060678

Academic Editor: Michal Fečkan

Received: 3 March 2021
Accepted: 19 March 2021
Published: 22 March 2021

1. Introduction

A moving load's effect on transport structures has been observed in literature since 1849. After the collapse of the Chester Rail Bridge in England in the year 1947, civil engineer R. Willis and mathematician G. G. Stokes published work [1,2] in which they tried to clarify the cause of the accident and a method for solving equations of motion describing the problem. Subsequently, a flood of articles appeared that tried to solve the problems of moving loads analytically, with varying degrees of applicability. The development of computer technologies has stimulated the transition from analytical to numerical methods of a solution. Initially, the effects of moving loads were addressed in the context of dynamic analysis of railway bridges, and gradually attention was paid to road bridges. A complete overview of the procedures up to 1959 is published in [3]. An overview of the moving load effects on road bridges up to 1975 is published in [4]. The Czech and Slovak Republics are known for their high-level theoretical approach to the solution of moving load effects on transport structures. The work of V. Koloušek and L. Frýba are known all over the world [5,6,7]. A generation of younger authors, who already use numerical methods in their solutions, followed up on the work of their teachers [8–11]. Over time, attention has shifted from bridges to roads and vehicles [12–14]. Computational models of vehicles with different degrees of aptness, quarter-1D models, half-2D models, and spatial-

3D models began to be developed. Single-layer or multi-layer models of asphalt or concrete pavements began to be created. Real unevenness of the road surface began to be taken into account. A contribution to the development was the appearance of FEM (Finite Element Method) on the scene. Finite methods have significantly expanded the possibilities of the solution. Matrix-oriented programming languages of a higher level than MATLAB [15] contributed to the development of numerical methods and the programming activities of engineers. The current situation in engineering practice is very inclined to solve interaction problems that have a theoretical and experimental foundation [16]. In general, it is stated that the research is aimed at solving increasingly complicated mathematical methods, which are used as a mathematical apparatus for solving these tasks. The final results of a theoretical task contain the large number of factors that are included in the calculation. If the problem is complicated, a detailed solution is needed to monitor and evaluate all aspects [17–20]. Monitoring, recording, and evaluating experimental measurements also form a very complicated part of the task. The process is time consuming and requires very precise work. However, it represents a possibility of verifying numerically obtained results. Therefore, the penetration of these two tasks is very valuable, and the results connected with it have a great weight in engineering and scientific practice [21–23].

There are many articles paying attention to numerical studies. Fewer papers are devoted to experimental studies. The contribution sought here is, as far as possible, to compare the results of numerical simulations of vehicle movement along the road with the results of experimental tests. This comparison will help engineers realize the current possibilities of applying numerical simulations in practice. It can also motivate them to look for new effective solutions. In the present state of knowledge, this work works with a combination of numerical and experimental analyses; with such a large amount of data study creates an original contribution to solving this engineering problem.

2. Computational Model of Vehicle

A multi-body computational model of vehicles can be created on three different qualitative levels: 1D–quarter model, 2D–plane model, and 3D–spatial model. Every model has its advantages and disadvantages, and under certain assumptions, it can be used as a solution for real practical problems [5]. The behavior of the multi-body computational model is described by a system of ordinary differential equations. The equations of motion can be derived in the sense of the component element method [24]. The relation between the components of displacements $\{\mathbf{r}(t)\}$, corresponding to individual degrees of freedom, and deformations of joining elements $\{\mathbf{d}(t)\}$ can be expressed by the transposed static matrix $[\mathbf{A}]^T$:

$$\{\mathbf{d}(t)\} = [\mathbf{A}]^T \{\mathbf{r}(t)\} \quad (1)$$

Dependence between elastic forces in joining elements (in the sense of the action of mass objects on joining elements) and its deformations is described by the equation

$$\{\mathbf{F}_{re}(t)\} = [\mathbf{k}] \{\mathbf{d}(t)\} \quad (2)$$

where **[k]** is the diagonal stiffness matrix of joining elements. Dependence of damping forces on the velocity of deformations $\{\dot{\mathbf{d}}(t)\}$ is described by the equation

$$\{\mathbf{F}_d(t)\} = [\mathbf{b}] \{\dot{\mathbf{d}}(t)\} \quad (3)$$

where **[b]** is a diagonal damping matrix. The derivation according to time t is denoted by a dot above the symbol. Friction forces are considered as

$$\begin{aligned} &\text{if } \{\dot{\mathbf{d}}(t)\} \geq +\dot{d}_c \ \{\mathbf{F}_f(t)\} = +\{\mathbf{f}\} \\ &\text{if } \{\dot{\mathbf{d}}(t)\} \geq -\dot{d}_c \ \{\mathbf{F}_f(t)\} = -\{\mathbf{f}\} \end{aligned} \quad (4)$$

$$\text{if abs}\left\{\dot{\mathbf{d}}(t)\right\} < +\dot{d}_c \;\; \{\mathbf{F_f}(t)\} = +\{\mathbf{f}\}^{\mathbf{T}}\left\{\dot{\mathbf{d}}(t)\right\}/\dot{d}_c$$

Resulting forces in joining elements in action on mass objects are

$$\{\mathbf{F_{JE}}(t)\} = -\{\mathbf{F_{re}}(t)\} - \{\mathbf{F_d}(t)\} - \{\mathbf{F_f}(t)\} \tag{5}$$

Sign (–) is due to the principle of action and reaction. From the forces in joining elements $\{\mathbf{F_{JE}}(t)\}$, the static equivalents corresponding to individual degrees of freedom $\{\mathbf{F_{DF}}(t)\}$ are calculated by

$$\{\mathbf{F_{DF}}(t)\} = \mathbf{[A]}\,\{\mathbf{F_{JE}}(t)\} \tag{6}$$

The gravity forces $\{\mathbf{F_G}\}$ and reactions in supports $\{\mathbf{F_{RS}}(t)\}$ must be added to the forces corresponding to individual degrees of freedom $\{\mathbf{F_{DF}}(t)\}$. In this manner we obtain the complete vector of forces $\{\mathbf{F_R}(t)\}$ acting on the computing model of vehicle:

$$\{\mathbf{F_R}(t)\} = \{\mathbf{F_{DF}}(t)\}+\{\mathbf{F_{DF,KO}}(t)\} = \{\mathbf{F_{DF}}(t)\}+\{\mathbf{F_G}\}+\{\mathbf{F_{RS}}(t)\} \tag{7}$$

The system of equations of motion describing the vibration of the computational model of vehicle is then expressed by the relation

$$[\mathbf{m}]\{\ddot{\mathbf{r}}(t)\} = \{\mathbf{F_R}(t)\} \tag{8}$$

where **[m]** is a diagonal mass matrix.

For this paper the spatial model of the vehicle was adopted, Figure 1. The model has 15 degrees of freedom and 10 joining elements. Tangible degrees of freedom (in number 9) correspond to movements of the mass points of the model, and intangible degrees of freedom (in number 6) correspond to movements of the contact points with the road. The displacement components of the individual points of the vehicle model (vector $\{\mathbf{r}(t)\}$) are numbered 1–15 (positive orientation is indicated by an arrow). The joining elements are numbered from 1 to 10 by numbers in rings. The individual columns of the matrix $\mathbf{[A]^T}$ represent the deformations of the joining elements as a result of the unit states of displacements (where one element of the vector $\{\mathbf{r}(t)\}$ is equal to 1 and the others are zero). The spatial model can capture the heave, pitch, and roll effects of the upper mass on the contact forces between the wheels and the runway.

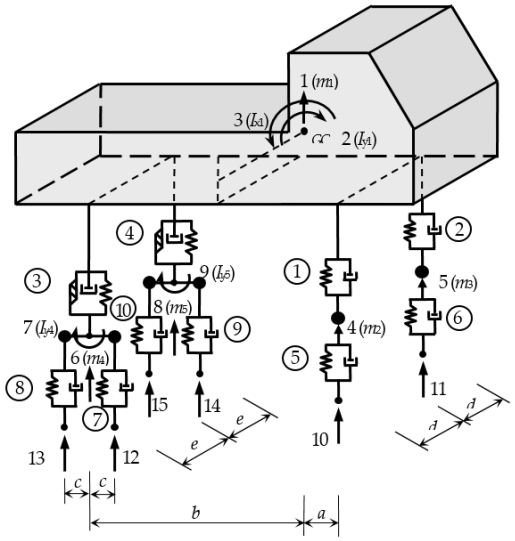

Figure 1. Computational model of vehicle.

The first step is to generate the vector $\{\mathbf{r}(t)\}$ and the matrix $\mathbf{[A]^T}$ that is dependent on it. The second step is to calculate the vector $\{\mathbf{d}(t)\}$.

$$\{\mathbf{r}\} = [r_1(t), r_2(t), r_3(t), r_4(t), r_5(t), r_6(t), r_7(t), r_8(t), r_9(t), u_5(t), u_6(t), u_7(t), u_8(t), u_9(t), u_{10}(t)]^{\mathbf{T}} \tag{9}$$

$$\{\mathbf{d}\} = [d_1(t), d_2(t), d_3(t), d_4(t), d_5(t), d_6(t), d_7(t), d_8(t), d_9(t), d_{10}(t)]^{\mathbf{T}} = [\mathbf{A}]^{\mathbf{T}}\{\mathbf{r}\} =$$

$$= \begin{bmatrix} 1 & -a & -d & -1 & 0 & 0 & 0 & 0 & 0 & 0 & 0 & 0 & 0 & 0 & 0 \\ 1 & -a & +d & 0 & -1 & 0 & 0 & 0 & 0 & 0 & 0 & 0 & 0 & 0 & 0 \\ 1 & +b & -e & 0 & 0 & -1 & 0 & 0 & 0 & 0 & 0 & 0 & 0 & 0 & 0 \\ 1 & +b & +e & 0 & 0 & 0 & 0 & -1 & 0 & 0 & 0 & 0 & 0 & 0 & 0 \\ 0 & 0 & 0 & +1 & 0 & 0 & 0 & 0 & 0 & -1 & 0 & 0 & 0 & 0 & 0 \\ 0 & 0 & 0 & 0 & +1 & 0 & 0 & 0 & 0 & 0 & -1 & 0 & 0 & 0 & 0 \\ 0 & 0 & 0 & 0 & 0 & +1 & -c & 0 & 0 & 0 & 0 & -1 & 0 & 0 & 0 \\ 0 & 0 & 0 & 0 & 0 & +1 & +c & 0 & 0 & 0 & 0 & 0 & -1 & 0 & 0 \\ 0 & 0 & 0 & 0 & 0 & 0 & 0 & +1 & -c & 0 & 0 & 0 & 0 & -1 & 0 \\ 0 & 0 & 0 & 0 & 0 & 0 & 0 & +1 & +c & 0 & 0 & 0 & 0 & 0 & -1 \end{bmatrix} \begin{Bmatrix} r_1(t) \\ r_2(t) \\ r_3(t) \\ r_4(t) \\ r_5(t) \\ r_6(t) \\ r_7(t) \\ r_8(t) \\ r_9(t) \\ u_5(t) \\ u_6(t) \\ u_7(t) \\ u_8(t) \\ u_9(t) \\ u_{10}(t) \end{Bmatrix} = \tag{10}$$

$$= \begin{Bmatrix} r_1(t) - a \cdot r_2(t) - d \cdot r_3(t) - r_4(t) \\ r_1(t) - a \cdot r_2(t) + d \cdot r_3(t) - r_5(t) \\ r_1(t) + b \cdot r_2(t) - e \cdot r_3(t) - r_6(t) \\ r_1(t) + b \cdot r_2(t) + e \cdot r_3(t) - r_8(t) \\ r_4(t) - u_5(t) \\ r_5(t) - u_6(t) \\ r_6(t) - c \cdot r_7(t) - u_7(t) \\ r_6(t) + c \cdot r_7(t) - u_8(t) \\ r_8(t) - c \cdot r_9(t) - u_9(t) \\ r_8(t) + c \cdot r_9(t) - u_{10}(t) \end{Bmatrix}$$

By mechanical multiplication of the matrices according to Equations (2) to (8), we obtain the needed Equation (11) by

$$[\mathbf{m}]\{\ddot{\mathbf{r}}(t)\} = \{\mathbf{F_R}(t)\}. \tag{11}$$

The mass matrix **[m]** in Equation (11) is diagonal. The elements of the main diagonal are presented in the row matrix $[\mathbf{m}]_{\mathbf{D}}$ (12). The last six elements are zero, since the computational model has also massless degrees of freedom $u_5(t)$, $u_6(t)$, $u_7(t)$, $u_8(t)$, $u_9(t)$, $u_{10}(t)$.

$$[\mathbf{m}]_{\mathbf{D}} = [m_1, I_{y1}, I_{x1}, m_2, m_3, m_4, I_{y4}, m_5, I_{y5}, 0,0,0,0,0,0]. \tag{12}$$

The first nine equations in the system (11) are equations of motion and the last six equations give the expressions for the reactions of the road:

$$\begin{aligned} \ddot{r}_1(t) = -\{&b_1 \cdot \dot{d}_1(t) + k_1 \cdot d_1(t) + b_2 \cdot \dot{d}_2(t) + k_2 \cdot d_2(t) + b_3 \cdot \dot{d}_3(t) + k_3 \cdot d_3(t) + \\ &+ b_4 \cdot \dot{d}_4(t) + k_4 \cdot d_4(t) + f_3 \cdot \dot{d}_3(t)/\dot{d}_c + f_4 \cdot \dot{d}_4(t)/\dot{d}_c\}/m_1, \\ \ddot{r}_2(t) = +\{&a \cdot (b_1 \cdot \dot{d}_1(t) + k_1 \cdot d_1(t)) + a \cdot (b_2 \cdot \dot{d}_2(t) + k_2 \cdot d_2(t)) - \end{aligned} \tag{13}$$

$$
\begin{aligned}
&-b\cdot(b_3\cdot\dot{d}_3(t)+f_3\cdot\dot{d}_3(t)/\dot{d}_c+k_3\cdot d_3(t))-\\
&-b\cdot(b_4\cdot\dot{d}_4(t)+f_4\cdot\dot{d}_4(t)/\dot{d}_c+k_4\cdot d_4(t))\}/I_{y1},\\
\ddot{r}_3(t)=&+\{d\cdot(b_1\cdot\dot{d}_1(t)+k_1\cdot d_1(t))-d\cdot(b_2\cdot\dot{d}_2(t)+k_2\cdot d_2(t))+\\
&+e\cdot(b_3\cdot\dot{d}_3(t)+f_3\cdot\dot{d}_3(t)/\dot{d}_c+k_3\cdot d_3(t))-\\
&-e\cdot(b_4\cdot\dot{d}_4(t)+f_4\cdot\dot{d}_4(t)/\dot{d}_c+k_4\cdot d_4(t))\}/I_{x1},\\
\ddot{r}_4(t)=&+\{b_1\cdot\dot{d}_1(t)+k_1\cdot d_1(t)-b_5\cdot\dot{d}_5(t)-k_5\cdot d_5(t)\}/m_2,\\
\ddot{r}_5(t)=&+\{b_2\cdot\dot{d}_2(t)+k_2\cdot d_2(t)-b_6\cdot\dot{d}_6(t)-k_6\cdot d_6(t)\}/m_3,\\
\ddot{r}_6(t)=&+\{b_3\cdot\dot{d}_3(t)+f_3\cdot\dot{d}_3(t)/\dot{d}_c+k_3\cdot d_3(t)-b_7\cdot\dot{d}_7(t)-k_7\cdot d_7(t)-b_8\cdot\dot{d}_8(t)-k_8\cdot d_8(t\\
\ddot{r}_7(t)=&+\{c\cdot(b_7\cdot\dot{d}_7(t)+k_7\cdot d_7(t))-c\cdot(b_8\cdot\dot{d}_8(t)+k_8\cdot d_8(t))\}/I_{y4}\\
\ddot{r}_8(t)=&+\{b_4\cdot\dot{d}_4(t)+f_4\cdot\dot{d}_4(t)/\dot{d}_c+k_4\cdot d_4(t)-b_9\cdot\dot{d}_9(t)-k_9\cdot d_9(t)-b_{10}\cdot\dot{d}_{10}(t)-k_{10}\cdot d_{1(}\\
\ddot{r}_9(t)=&+\{c\cdot(b_9\cdot\dot{d}_9(t)+k_9\cdot d_9(t))-c\cdot(b_{10}\cdot\dot{d}_{10}(t)+k_{10}\cdot d_{10}(t))\}/I_{y5}.
\end{aligned}
$$

$$
\begin{aligned}
F_{RS,5}(t)&=(\frac{m_1}{2}\cdot\frac{b}{s}+m_2)\cdot g-(b_5\cdot\dot{d}_5(t)+k_5\cdot d_5(t)),\\
F_{RS,6}(t)&=(\frac{m_1}{2}\cdot\frac{b}{s}+m_3)\cdot g-(b_6\cdot\dot{d}_6(t)+k_6\cdot d_6(t)),\\
F_{RS,7}(t)&=(\frac{m_1}{4}\cdot\frac{a}{s}+\frac{m_4}{2})\cdot g-(b_7\cdot\dot{d}_7(t)+k_7\cdot d_7(t)),\\
F_{RS,8}(t)&=(\frac{m_1}{4}\cdot\frac{a}{s}+\frac{m_4}{2})\cdot g-(b_8\cdot\dot{d}_8(t)+k_8\cdot d_8(t)),\\
F_{RS,9}(t)&=(\frac{m_1}{4}\cdot\frac{a}{s}+\frac{m_5}{2})\cdot g-(b_9\cdot\dot{d}_9(t)+k_9\cdot d_9(t)),\\
F_{RS,10}(t)&=(\frac{m_1}{4}\cdot\frac{a}{s}+\frac{m_5}{2})\cdot g-(b_{10}\cdot\dot{d}_{10}(t)+k_{10}\cdot d_{10}(t)).
\end{aligned}
\tag{14}
$$

3. Road Unevenness

Road unevenness is the source of vehicle kinematic excitation. It is an integral part of the numerical solution of the vehicle response. It is possible to generate a random road profile of a certain category A–H according to the international standard (ISO 8606) [25] or to map unevenness on the selected section of the road. For this article, the geodetic method of exact leveling was used to identify road unevenness. Vertical road unevenness was measured in 0.25 m increments on a 110 m long section in two profiles, left and right, 2 m apart. The road has a small slope, 0.48%. In numerical calculations, the slope of the road is neglected. The left and right road profiles are shown in Figure 2.

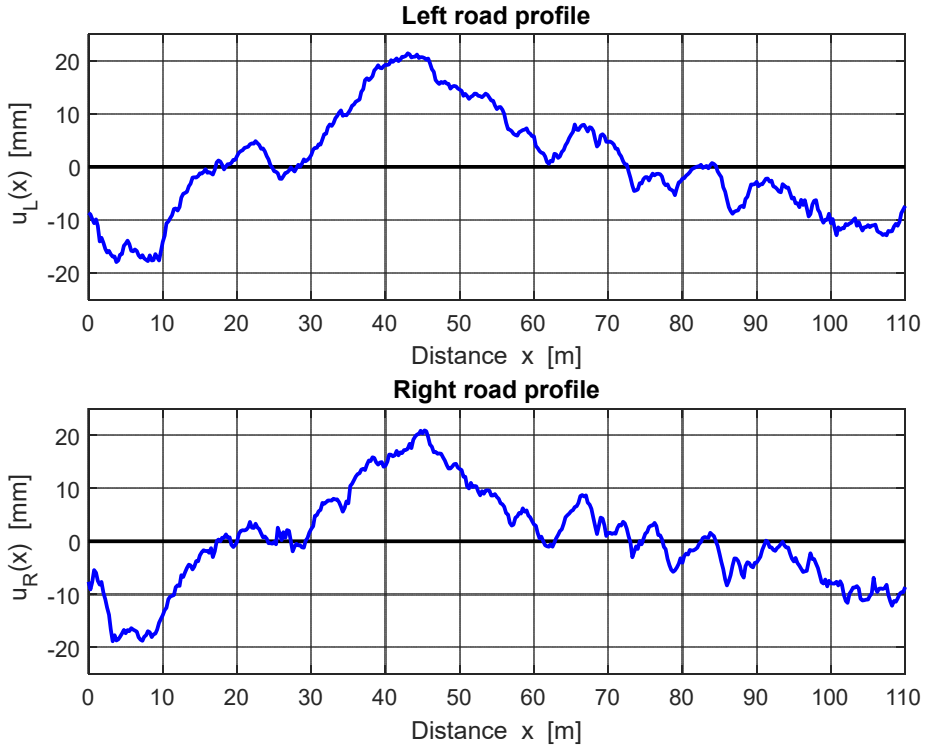

Figure 2. Left and right road profiles.

Road unevenness is random. Unevenness in the monitored section on the left and right longitudinal road profile represents only one implementation of the random process. The basic statistical characteristics that characterize the longitudinal profile from a statistical point of view are given in Table 1.

Table 1. Statistical characteristics of the road profiles.

	u_L	u_R
Mean value $\overline{u}$	0.5874 mm	0.3812 mm
Arithmetic mean deviation R_a	8.1329 mm	7.0686 mm
Root mean square (*RMS*) average deviation R_q	10.0791 mm	9.0668 mm
Dispersion σ^2	101.5884 mm^2	82.2073 mm^2
Effective value *RMS*	10.0962 mm	9.0748 mm
Asymmetry coefficient R_{sk}	0.2454	0.1128
Kurtosis R_{ku}	2.3314	2.6591
The greatest depth of unevenness	−17.9348 mm	−18.8316 mm
The largest height of unevenness	21.4085 mm	20.9047 mm
Overall height of the profile	39.3433 mm	39.7364 mm

It is generally accepted that vertical road unevenness satisfies Gauss's law of probability distribution. A visual view of this assumption can be made from Figure 3, where the probability distribution histograms for vertical unevenness in the left and right longitudinal road profiles are compared to Gauss's law. It should be noted that the length of the 110 m section is too short for such a comparison to be made seriously.

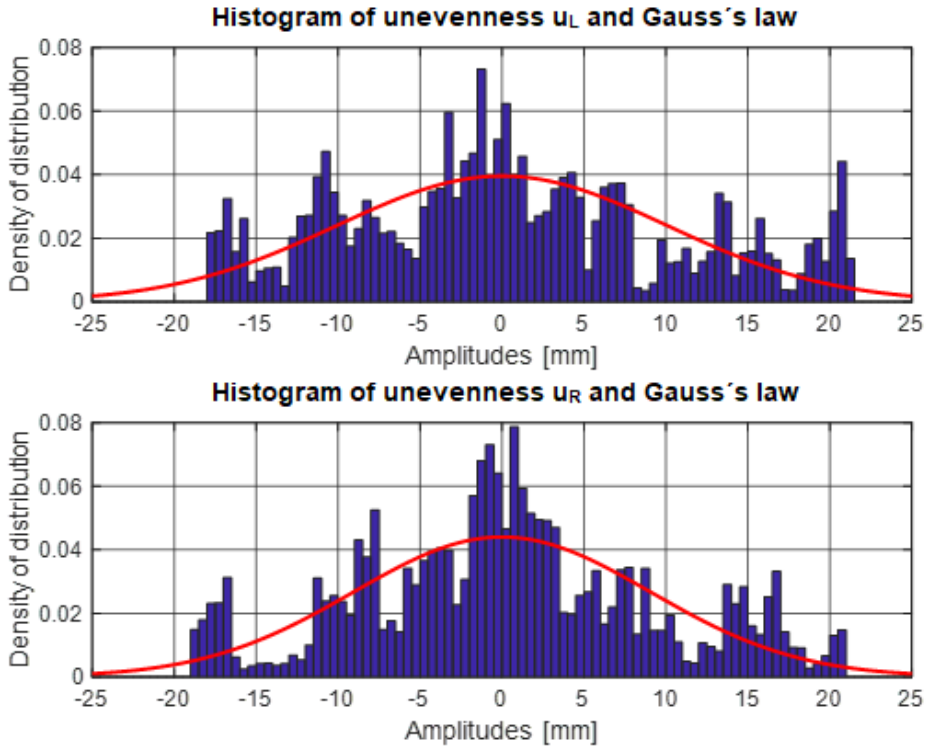

Figure 3. Histogram of unevenness and Gauss's law.

The quality of a road surface is assessed by an international standard [7] that divides roads into 8 categories A to H according to the values of power spectral densities (PSD). The smoothed PSD $S_u(\Omega)$ can be approximated in a log-log scale by a straight line. It is valid that

$$\log S_u(\Omega) = \log S_u(\Omega_0) - k \cdot (\log\Omega - \log\Omega_0) \quad (15)$$

or also

$$S_u(\Omega) = S_u(\Omega_0) \cdot \left(\frac{\Omega}{\Omega_0}\right)^{-k} \quad (16)$$

where Ω is path angular frequency in [1/m], Ω_0 = 1 [1/m] is reference angular frequency, and k = 2. Figures 4 and 5 show the PSD of the left and right road profile on the log-log scale. The road can be included in category B.

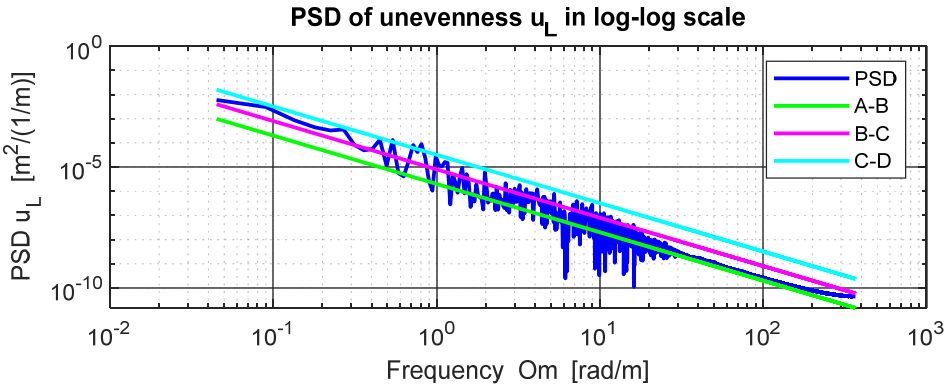

Figure 4. Power spectral density (PSD) of left road profile in log-log scale.

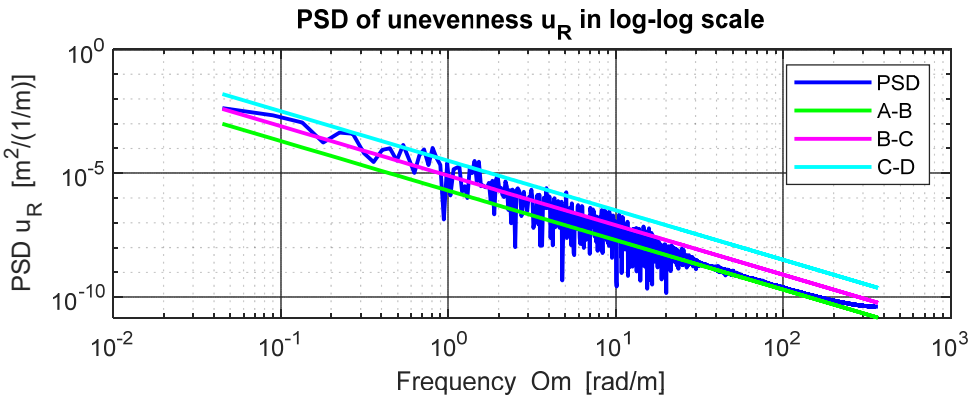

Figure 5. PSD of right road profile in log-log scale.

4. Numerical Simulation of Vehicle Movement along a Road

A computer program in the MATLAB was developed for numerical simulation of vehicle movement along the road. Because it is a discrete computational model, the problem is described by a system of ordinary differential equations. The system of Equation (11) breaks down into two systems. The equations corresponding to the mass degrees of freedom in Equation (9) represent the equations of motion themselves in Equation (13), which are the subject of a numerical solution. The equations corresponding to the massless degrees of freedom in Equation (6) represent the equations for calculating the subsoil reactions in Equation (14). The second-order equations of motion are replaced by the first-order equations with the help of suitable substitution:

$$\{\mathbf{r}(t)\} = \{\mathbf{y_1}(t)\} \tag{17}$$

$$\{\dot{\mathbf{r}}(t)\} = \{\mathbf{y_2}(t)\} \rightarrow \{\dot{\mathbf{y}}_2(t)\} = \{\ddot{\mathbf{r}}(t)\} \tag{18}$$

The subject of the solution is then the system of the first-order equations of the type

$$\{\dot{\mathbf{y}}_1(t)\} = \{\mathbf{y_2}(t)\} \tag{19}$$

$$\{\dot{\mathbf{y}}_2(t)\} = \{\ddot{\mathbf{r}}(t)\} \tag{20}$$

The ode45 procedure was used to solve the system of differential Equations (19) and (20). Relative error tolerance RelTol = 1×10^{-3}, absolute error tolerance AbsTol = 1×10^{-6}. The output of the numerical integration was realized in steps of 0.0005 s, which corresponds to a sampling frequency of 2000 Hz. At the beginning of the simulation at time $t = 0$, the vehicle is at a rest in a state of static equilibrium and is in contact with the road. The rear axle is at the beginning of the monitored road section. At the end of the simulation, the front axle is at the end of the monitored section. The vehicle moves at a constant speed throughout the section. The total weight of the vehicle is 21,500 kg. The damping in the vehicle tires is neglected in the simulation.

The output of the simulation is the time courses of all kinematic quantities (deflections, speeds, accelerations) in the characteristic points of the vehicle and the contact forces between the wheel of the vehicle and the road. The list of monitored quantities is as follows:

$r_1(t)$-vertical deflection of the center of gravity of the sprung mass of the vehicle.
$r_2(t)$-the angle of rotation of the vehicle's sprung mass in the longitudinal direction about an axis passing through the center of gravity.
$r_3(t)$-the angle of rotation of the vehicle's sprung mass in a transverse direction about an axis passing through the center of gravity.
$r_4(t)$-vertical deflection of the right front axle of the vehicle.
$r_5(t)$-vertical deflection of the left front axle of the vehicle.

$r_6(t)$-vertical deflection of the right rear axle of the vehicle.
$r_7(t)$-the angle of rotation of the right rear axle in the longitudinal direction.
$r_8(t)$-vertical deflection of the left rear axle of the vehicle.
$r_9(t)$-the angle of rotation of the left rear axle in the longitudinal direction.
$F_5(t)$-contact force between the right front wheel and the road.
$F_6(t)$-contact force between the left front wheel and the road.
$F_7(t)$-contact force between the right front wheel of the rear axle and the road.
$F_8(t)$-contact force between the right rear wheel of the rear axle and the road.
$F_9(t)$-contact force between the left front wheel of the rear axle and the road.
$F_{10}(t)$-contact force between the left rear wheel of the rear axle and the road.

It is possible to quantify velocities $\dot{r}_i(t) \equiv r_{di}, (i = 1,2, \ldots, 9)$ and accelerations $\ddot{r}_i(t) \equiv r_{ddi}, (i = 1,2, \ldots, 9)$ for all monitored kinematic quantities. Figures 6–10 show examples of time courses of selected quantities for a vehicle at a speed of 43.2 km/h.

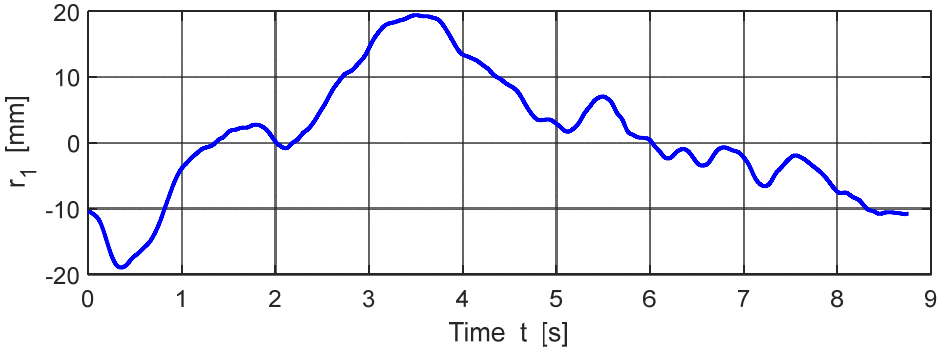

Figure 6. Vertical deflection of the center of gravity of the sprung mass of vehicle.

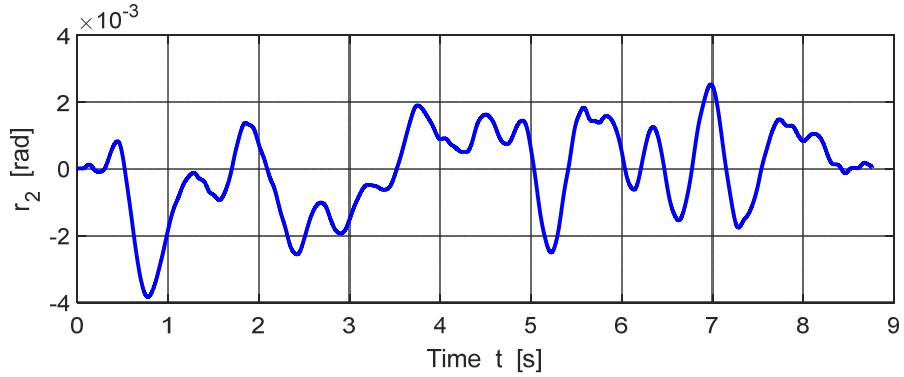

Figure 7. Angle of rotation of the sprung mass of vehicle in the longitudinal direction about an axis passing through the center of gravity.

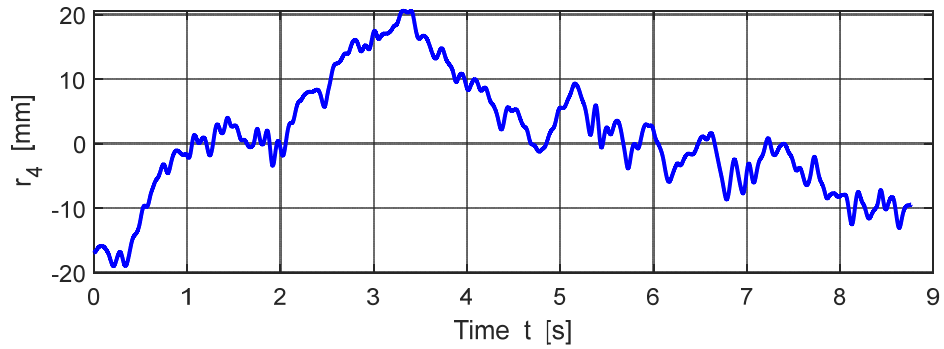

Figure 8. Vertical deflection of the right front axle of vehicle.

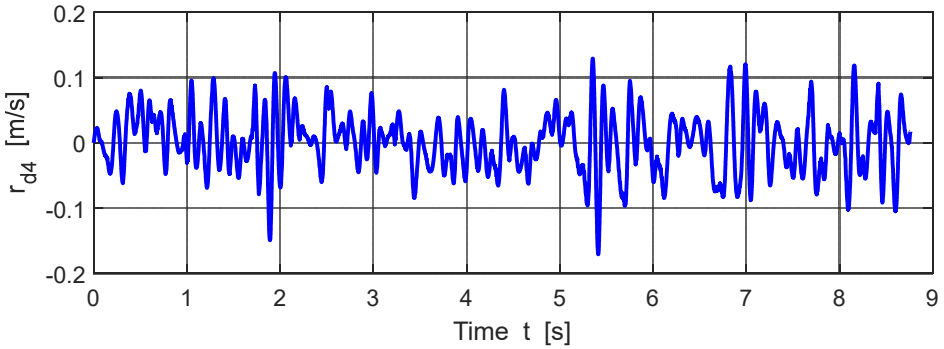

Figure 9. Speed of vertical motion of the right front axle of vehicle.

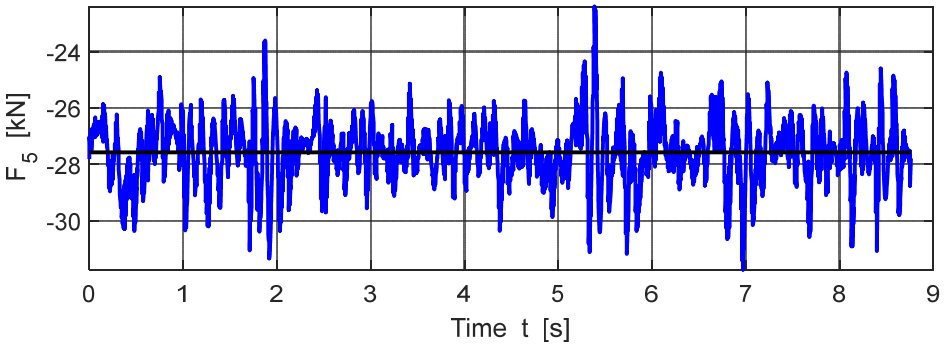

Figure 10. Contact force between the left rear wheel of the rear axle and the road.

5. Results

To assess the degree of the correctness of the numerical simulation of the vehicle response when the vehicle moves along the road, experimental tests were realized. The experiment was performed with a Tatra T815 vehicle whose parameters were used in the numerical simulation process. During the test, vertical accelerations were monitored at three points on the right side of the vehicle: at the center of gravity (CG) of the vehicle's sprung mass-sensor, A1; on the right front axle (FA)-sensor, A2; and on the right rear axle (RA)-sensor A3. See Figure 11.

Acceleration sensors Brüel & Kjær type BK4508B were used to monitor the response. The measuring string was composed of these components: sensor, amplifier with a band-pass filter, analog–digital interface, computer. The signal from the sensor was routed through a coaxial cable. A detailed view of the sensor and its location on the front and rear axles are shown in Figure 12. The measuring string was located in the vehicle. The sampling frequency was 2000 Hz.

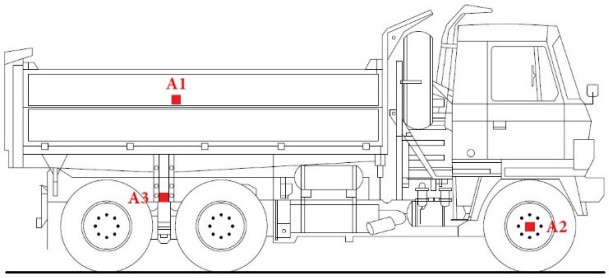

Figure 11. Localization of sensors on the vehicle.

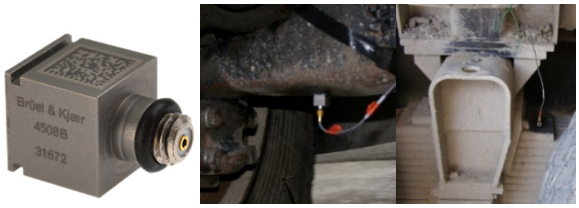

Figure 12. Sensor and its location on the front and rear axles.

The length of the monitored section of the road was 100 m. On this section of road, the average vehicle speed was measured as follows: steel strips and accelerometers (D2 and D3) were placed on the road in the transverse direction at a distance of 100 m, Figure 13.

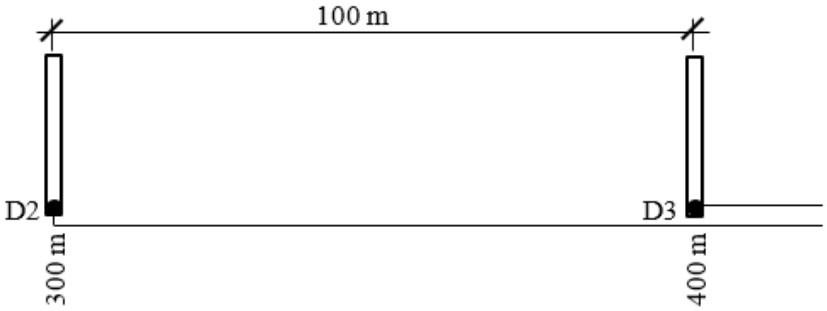

Figure 13. Steel strips with accelerometers D2 and D3 at a distance of 100 m.

The average speed was calculated from the known distance and travel time. The passage of the wheel through the steel strip is manifested as a sharp impulse in the accelerometer record. By comparing the records of accelerometers D2 and D3, it is possible to determine the travel time, Figure 14. Travel time t_t is determined as the difference between the end time t_e and the start time t_s of the passage, $t_t = t_e - t_s$. The average speed of the vehicle is determined as the ratio of the section length and the passage time, $v = l_s/t_t$. The time record from the sensors on the road was synchronized with the time record from the sensors on the vehicle. A total of 12 vehicle runs were performed in the experiment at different speeds, from 15.18 km/h to 52.95 km/h.

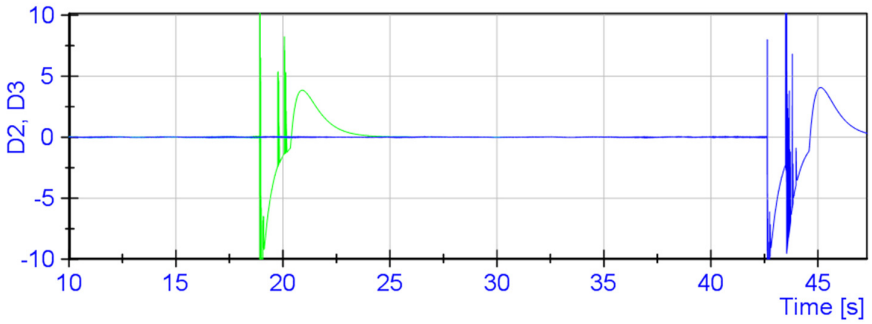

Figure 14. Records from accelerometers D2 and D3.

6. Comparison of Numerically and Experimentally Obtained Results

During the experiment, the vehicle passed along the road at a specific speed. The same phenomenon was simulated by numerical simulation. From the records of vehicle response obtained by the experiment and by numerical simulation, sections corresponding to the vehicle movement along the selected section of road in the length of 100 m were selected. These selected sections were subjected to mutual comparison. Runs at the lowest

speed $V = 15.18$ km/h and at the highest speed $V = 52.95$ km/h were chosen for comparison. The values of the vertical accelerations at three points on the right side of the vehicle were compared at the center of gravity of the vehicle's sprung mass-sensor A1, on the front axle-sensor A2, and on the rear axle-sensor A3.

First, a comparison of the monitored quantities at the vehicle speed $V = 15.18$ km/h is presented. Time records lasted 23.71 s and contained 47,421 samples. Figure 15 shows a visual comparison of the vertical accelerations at the center of gravity of the sprung mass of the vehicle obtained experimentally and numerically.

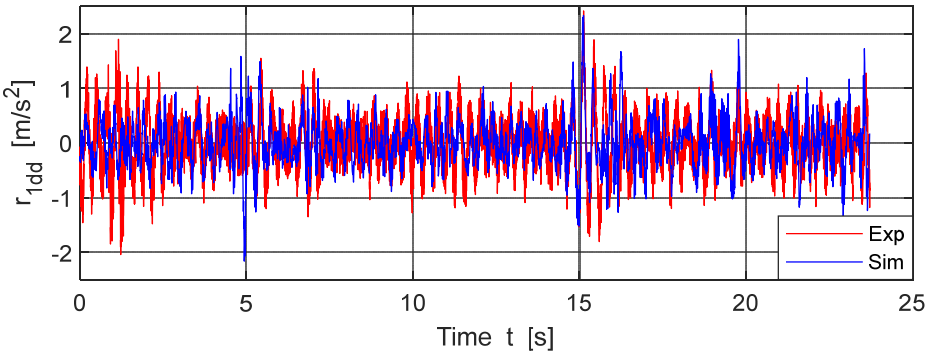

Figure 15. Acceleration in the center of gravity (CG) of vehicle sprung mass, $V = 15.18$ km/h.

The kinematic excitation was random, so the response of the vehicle was also random. One passage of the vehicle represents only one realization of the random process. From this point of view, it did not make sense to compare the values of the two records at each point. It was more realistic to compare the basic statistical characteristics of both records. Table 2 compares the basic statistical characteristics for experimentally and numerically obtained values of vertical accelerations at the center of gravity of the vehicle sprung mass.

Table 2. Statistical characteristics of acceleration in vehicle CG.

	Experiment	**Simulation**
Mean value $\bar{a}$	−0.0019 mm	−0.0008 mm
Arithmetic mean deviation R_a	0.3632 mm	0.3469 mm
Root mean square average deviation R_q	0.4688 mm	0.4575 mm
Dispersion σ^2	0.2198 mm^2	0.2093 mm^2
Effective value *RMS*	0.4688 mm	0.4575 mm
Asymmetry coefficient R_{sk}	0.4408	0.3230
Kurtosis R_{ku}	3.7620	4.8537
The greatest depth of record	−2.0433 mm	−2.1635 mm
The largest height of record	2.4146 mm	2.3314 mm
Overall height of the record	4.4579 mm	4.4950 mm

The density of probability distribution or distribution function provide complete information about the random variable. Therefore, in the next step, these characteristics are compared with each other, Figures 16 and 17.

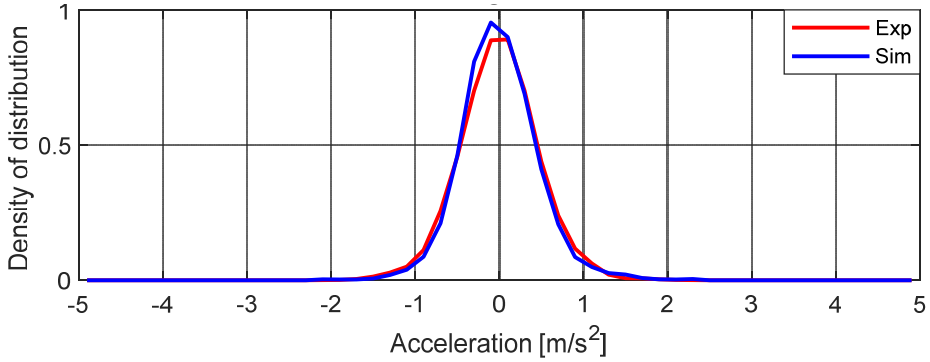

Figure 16. Density of probability distribution, acceleration in vehicle CG.

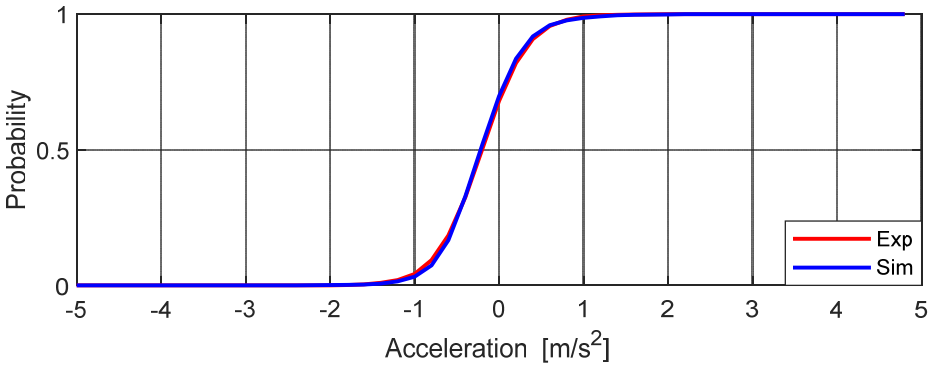

Figure 17. Distribution function, acceleration in vehicle CG.

Frequency spectra are needed to evaluate the dynamic behavior of structures in the frequency domain. Power spectral densities (PSD) are often used. In the next step, the PSDs were also compared with each other. The Fast Fourier Transform (FFT) was used to calculate the frequency spectra. The FFT works with the number of 2^n samples, so 2^{15} = 32,768 samples from the beginning of acceleration records were selected for the analysis. As we can see from Figure 18, the dominant frequencies were in the range of 0–10 Hz, so the PSD was compared in this frequency range. The comparison of the PSDs of the vertical accelerations at the center of gravity of the vehicle sprung mass for experimentally and numerically obtained records is shown in Figure 19.

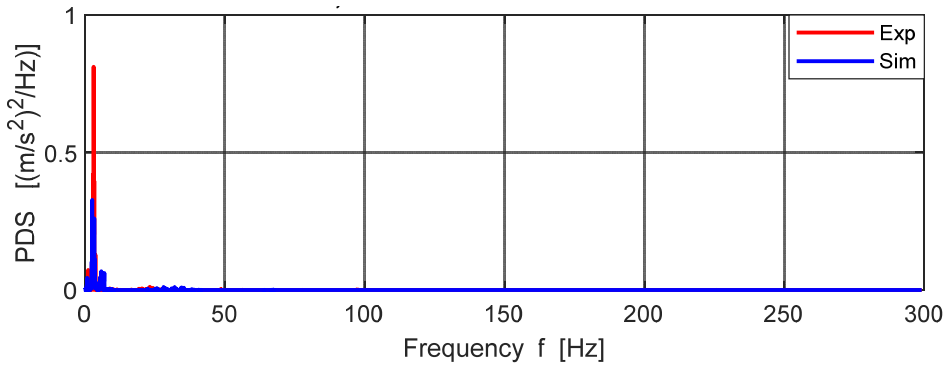

Figure 18. PSD of vertical accelerations in vehicle CG.

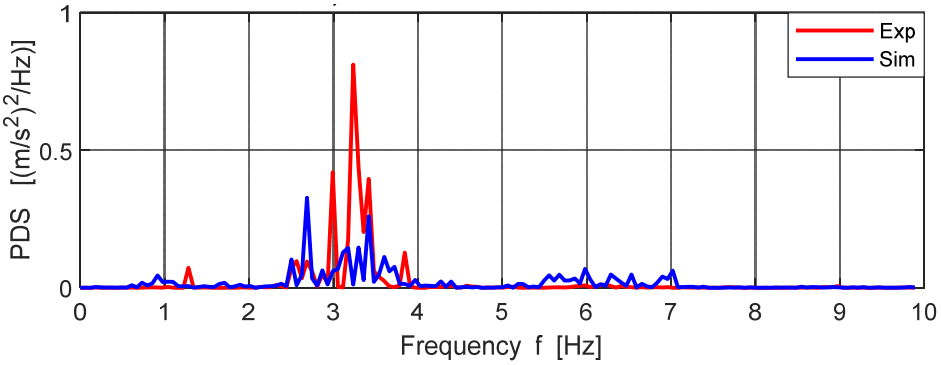

Figure 19. PSD of vertical accelerations in vehicle CG, 0–10 Hz.

Although the frequency clusters for both records are similar, the powers of individual frequencies in the simulated record were significantly lower.

The acceleration records on the right front axle were compared similarly. Figure 20 shows a visual comparison of vertical accelerations on the right front axle.

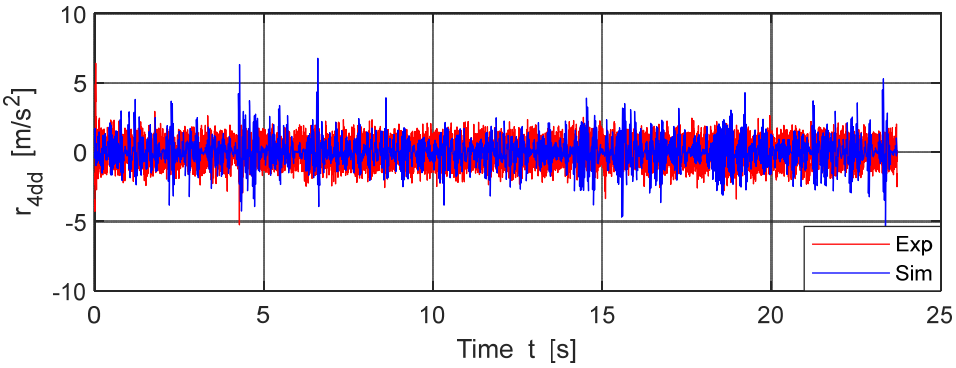

Figure 20. Acceleration on right front axle, V = 15.18 km/h.

Table 3 compares the basic statistical characteristics for experimentally and numerically obtained values of vertical accelerations on the right front axle. The density of probability distribution and distribution function are compared in Figures 21 and 22.

Table 3. Statistical characteristics of acceleration on right front axle.

	Experiment	**Simulation**
Mean value $\bar{a}$	0.0031 mm	−0.0008 mm
Arithmetic mean deviation R_a	0.5311 mm	0.5878 mm
Root mean square average deviation R_q	0.6786 mm	0.8324 mm
Dispersion σ^2	0.4605 mm²	0.6929 mm²
Effective value *RMS*	0.6786 mm	0.8324 mm
Asymmetry coefficient R_{sk}	0.0809	0.1851
Kurtosis R_{ku}	4.7239	6.8217
The greatest depth of record	−5.2235 mm	−5.6434 mm
The largest height of record	6.4155 mm	6.7649 mm
Overall height of the record	11.6390 mm	12.4084 mm

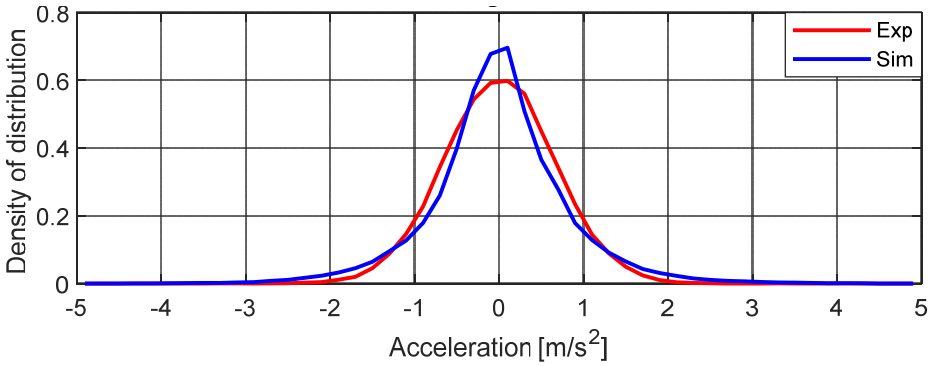

Figure 21. Density of probability distribution, acceleration on vehicle front axle (FA).

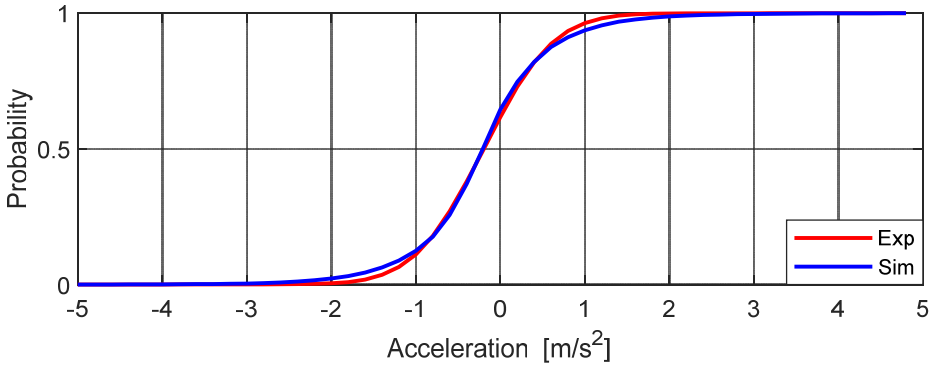

Figure 22. Distribution function, acceleration on vehicle FA.

The comparison of PDSs is shown in Figure 23. The dominant frequencies were located in the frequency range of 0–25 Hz. Although the same frequency components appear in both records, their powers were completely different.

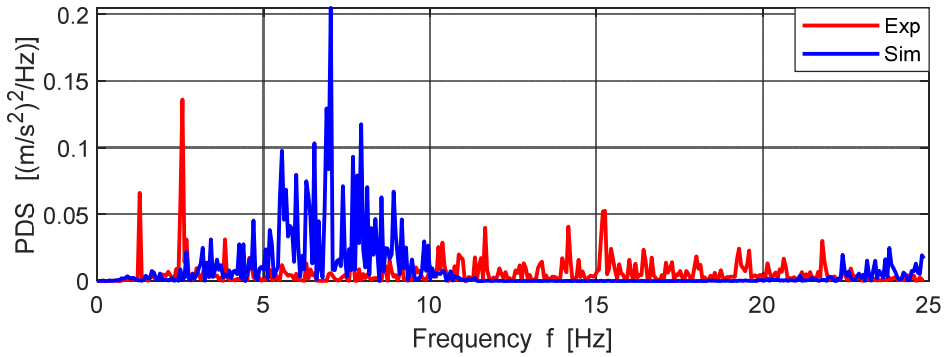

Figure 23. PSD of vertical accelerations on vehicle FA, 0–25 Hz.

In the third, the vertical accelerations on the right rear axle were also compared. Figure 24 shows a visual comparison of vertical accelerations on the right rear axle.

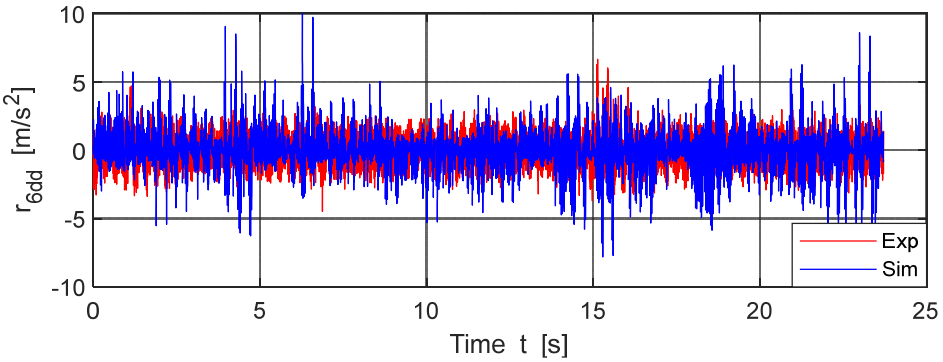

Figure 24. Acceleration on right rear axle, V = 15.18 km/h.

Table 4 compares the basic statistical characteristics for experimentally and numerically obtained values of vertical accelerations on the right rear axle. The density of probability distribution and distribution function are compared in Figures 25 and 26.

Table 4. Statistical characteristics of acceleration on right rear axle.

	Experiment	**Simulation**
Mean value $\bar{a}$	−0.0062 mm	−0.0003 mm
Arithmetic mean deviation R_a	0.7076 mm	0.8128 mm
Root mean square average deviation R_q	0.9106 mm	1.1605 mm
Dispersion σ^2	0.8292 mm^2	1.3468 mm^2
Effective value *RMS*	0.9106 mm	1.1605 mm
Asymmetry coefficient R_{sk}	0.2835	0.1368
Kurtosis R_{ku}	4.5032	7.6179
The greatest depth of record	−4.6194 mm	−7.8089 mm
The largest height of record	6.6533 mm	10.1296 mm
Overall height of the record	11.2728 mm	17.9385 mm

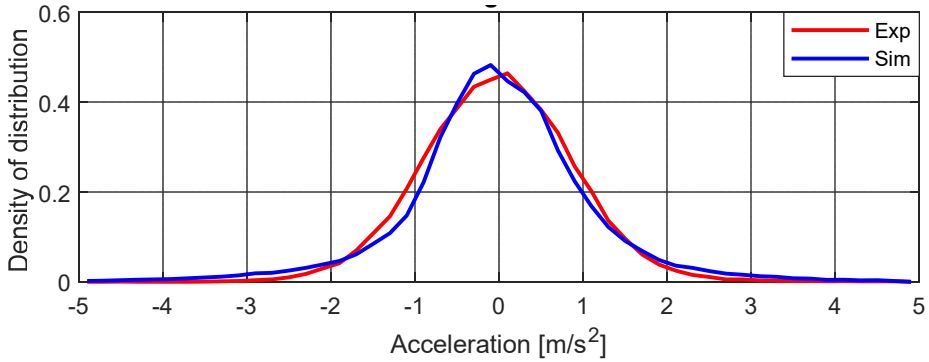

Figure 25. Density of probability distribution, acceleration on vehicle rear axle (RA).

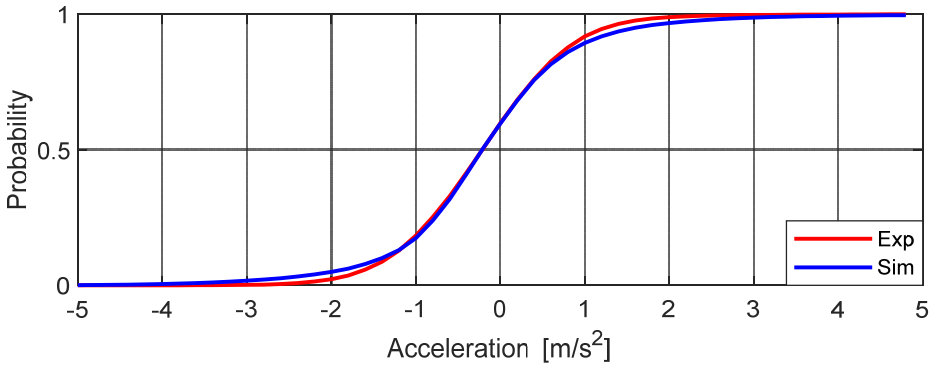

Figure 26. Distribution function, acceleration on vehicle RA.

The comparison of PDSs in the frequency range of 0–10 Hz is made in Figure 27.

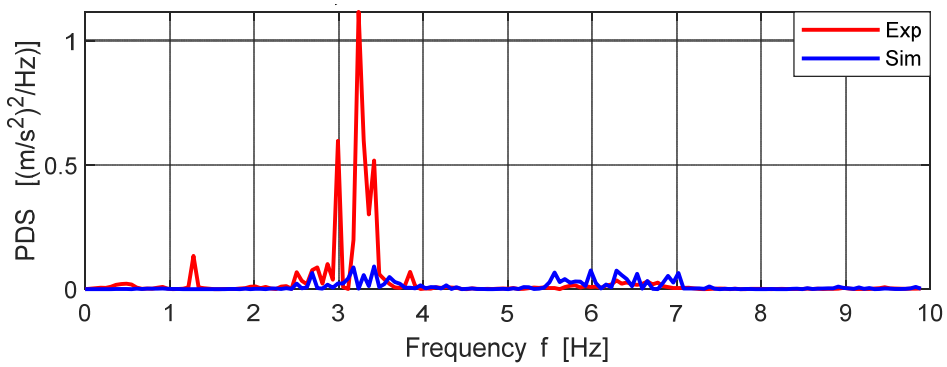

Figure 27. PSD of vertical accelerations on vehicle RA, 0–10 Hz.

All kinematic values of the vehicle response depend on the speed of movement of the vehicle. Speed is the most important parameter entering into the vehicle–road interaction. It only makes sense to talk about the influence of all other parameters in connection with a certain specific speed of the vehicle. Therefore, in the following text, a comparison is made for a higher vehicle speed V = 52.95 km h. Time records lasted 6.7985 s and contained 13,598 samples. Figure 28 shows a visual comparison of vertical accelerations in the center of gravity of the sprung mass of the vehicle.

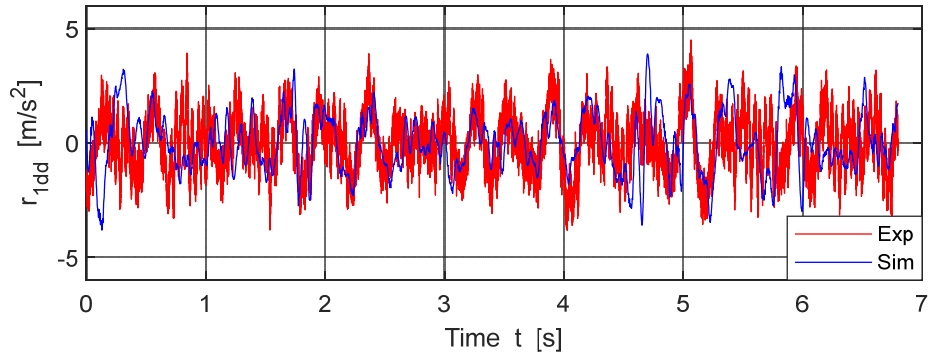

Figure 28. Acceleration in the CG of vehicle sprung mass, V = 52.85 km/h.

Table 5 compares the basic statistical characteristics for experimentally and numerically obtained values of vertical accelerations at the center of gravity of the vehicle. The density of the probability distribution and distribution function are compared in Figures 29 and 30.

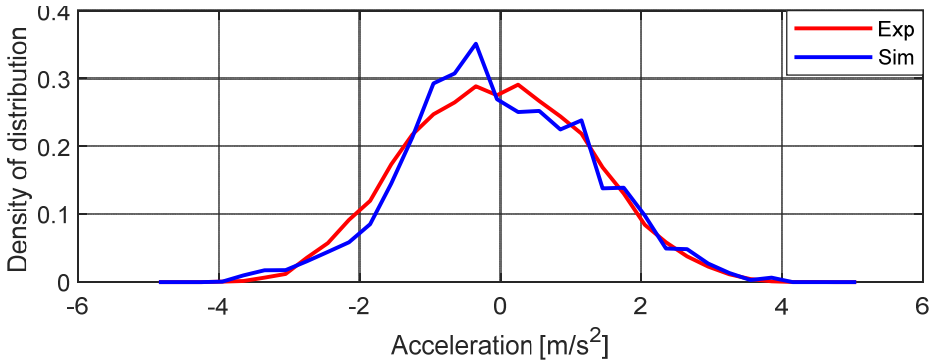

Figure 29. Density of probability distribution, acceleration in vehicle CG.

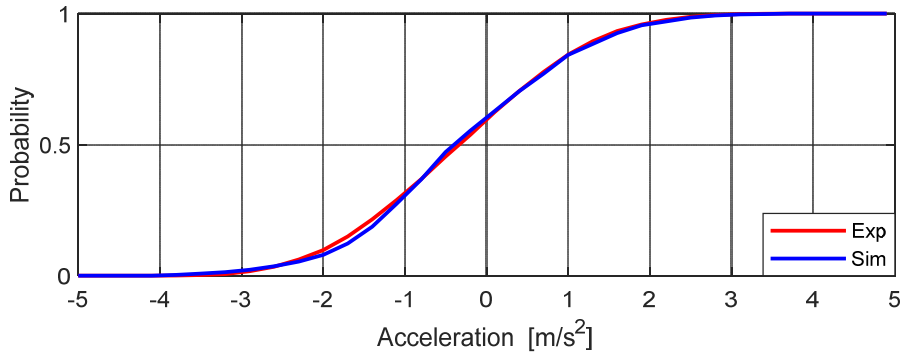

Figure 30. Distribution function, acceleration in vehicle CG.

Table 5. Statistical characteristics of acceleration in vehicle CG.

	Experiment	Simulation
Mean value $\bar{a}$	−0.0296 mm	−0.0060 mm
Arithmetic mean deviation R_a	1.0412 mm	1.0346 mm
Root mean square average deviation R_q	1.2769 mm	1.2843 mm
Dispersion σ^2	1.6307 mm^2	1.6495 mm^2
Effective value *RMS*	1.2773 mm	1.2843 mm
Asymmetry coefficient R_{sk}	0.0532	0.0676
Kurtosis R_{ku}	2.6251	2.9134
The greatest depth of record	−3.8163 mm	−3.8200 mm
The largest height of record	4.5049 mm	3.8873 mm
Overall height of the record	8.3213 mm	7.7074 mm

The acceleration record had 13,598 samples. To calculate the frequency spectrum, we needed 2^n samples, that is, either 8192 or 16,384. We decided on 16,384 samples, and the missing 2786 samples were filled with zeros. The comparison of PDSs in the frequency range 0–10 Hz is shown in Figure 31.

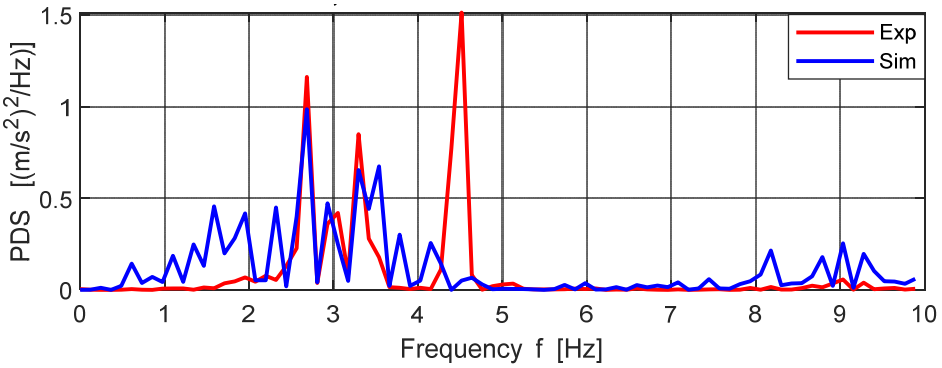

Figure 31. PSD of vertical accelerations in vehicle CG, 0–10 Hz.

In the next step, the vertical accelerations on the right front axle were compared. Figure 32 shows a visual comparison of vertical accelerations on the right front axle.

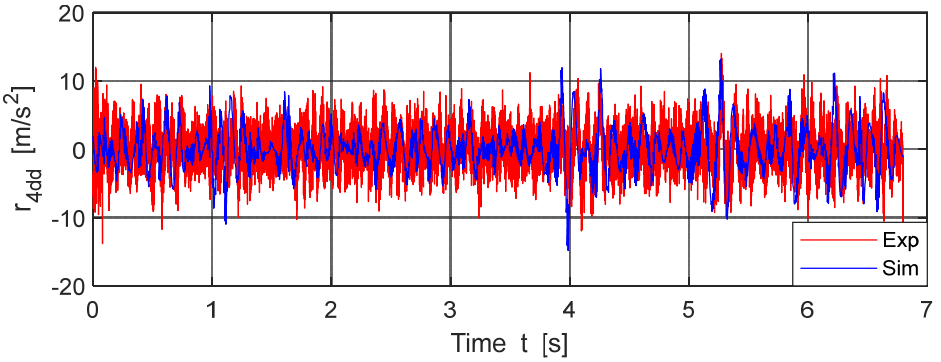

Figure 32. Acceleration on right front axle, V = 52.95 km/h.

Table 6 compares the basic statistical characteristics for experimentally and numerically obtained values of vertical accelerations on the right front axle. The density of probability distribution and distribution function are compared in Figures 33 and 34. The comparison of PDSs in the frequency range 0–10 Hz is shown in Figure 35.

Table 6. Statistical characteristics of acceleration on vehicle FA.

	Experiment	**Simulation**
Mean value $\bar{a}$	0.0396 mm	−0.0076 mm
Arithmetic mean deviation R_a	2.4080 mm	2.3237 mm
Root mean square average deviation R_q	3.0531 mm	3.1212 mm
Dispersion σ^2	9.3214 mm^2	9.7419 mm^2
Effective value *RMS*	3.0533 mm	3.1212 mm
Asymmetry coefficient R_{sk}	0.0934	0.1137
Kurtosis R_{ku}	3.3311	4.3811
The greatest depth of record	−13.8083 mm	−14.8321 mm
The largest height of record	14.0480 mm	13.1869 mm
Overall height of the record	27.8563 mm	28.0191 mm

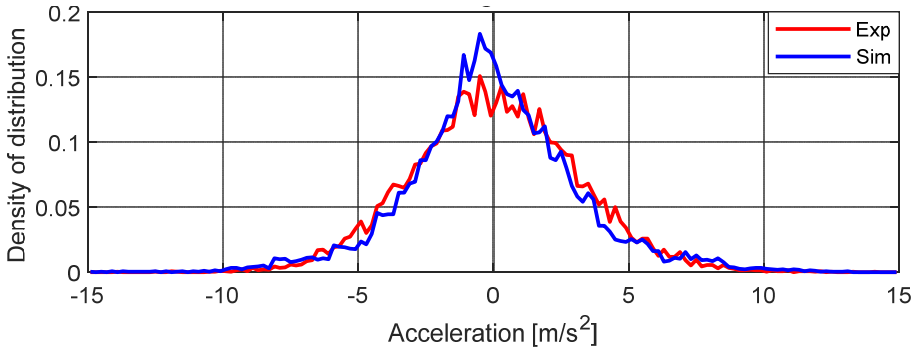

Figure 33. Density of probability distribution, acceleration on vehicle FA.

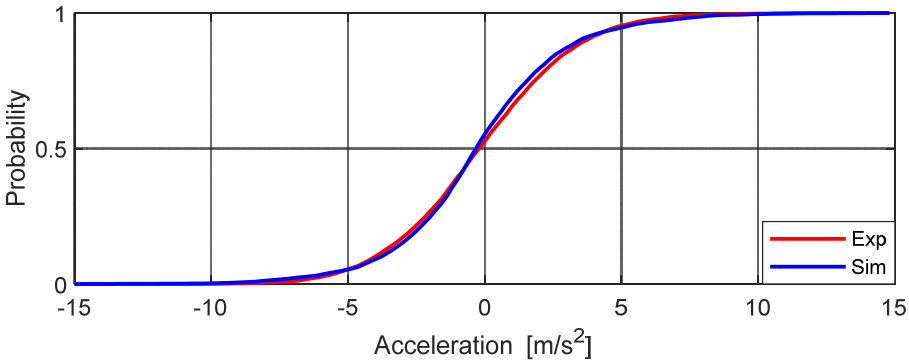

Figure 34. Distribution function, acceleration on vehicle FA.

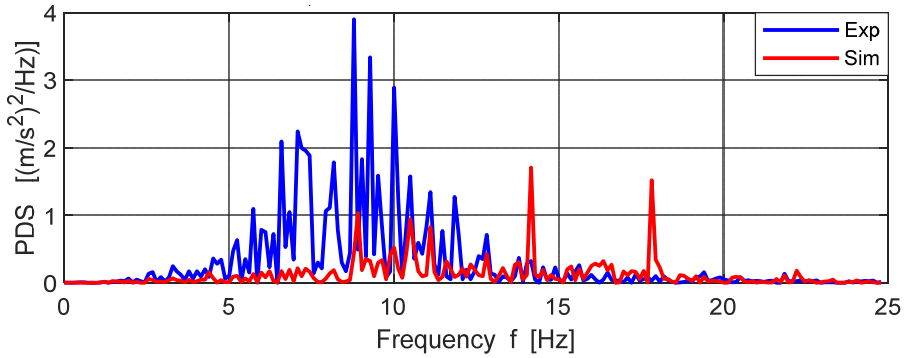

Figure 35. PSD of vertical accelerations on vehicle FA, 0 –25 Hz.

In the last step, the vertical accelerations on the right rear axle were compared. Figure 36 shows a visual comparison of vertical accelerations on the right rear axle.

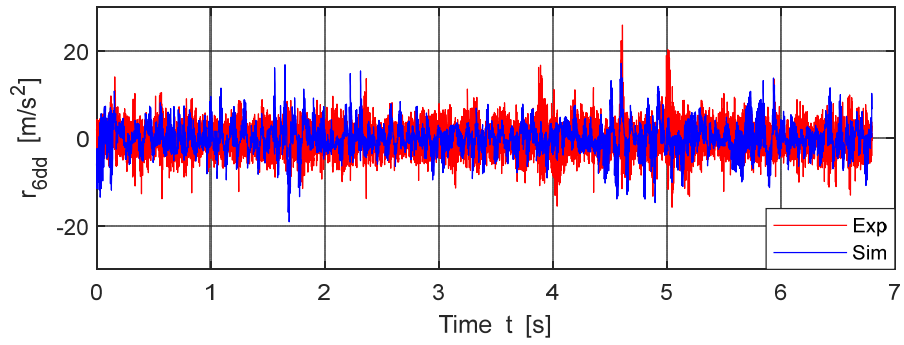

Figure 36. Acceleration on right rear axle, V = 52.95 km/h.

Table 7 compares the basic statistical characteristics for experimentally and numerically obtained values of vertical accelerations on the right rear axle. The density of probability distribution and distribution function are compared in Figures 37 and 38.

Table 7. Statistical characteristics of acceleration on vehicle RA.

	Experiment	Simulation
Mean value $\bar{a}$	−0.1588 mm	−0.0184 mm
Arithmetic mean deviation R_a	2.4934 mm	2.4533 mm
Root mean square average deviation R_q	3.2557 mm	3.2746 mm
Dispersion σ^2	10.5998 mm^2	10.7233 mm^2
Effective value *RMS*	3.2596 mm	3.2746 mm
Asymmetry coefficient R_{sk}	0.2650	0.1038
Kurtosis R_{ku}	5.1084	4.8027
The greatest depth of record	−15.7769 mm	−19.1264 mm
The largest height of record	25.9766 mm	17.1971 mm
Overall height of the record	41.7536 mm	36.3236 mm

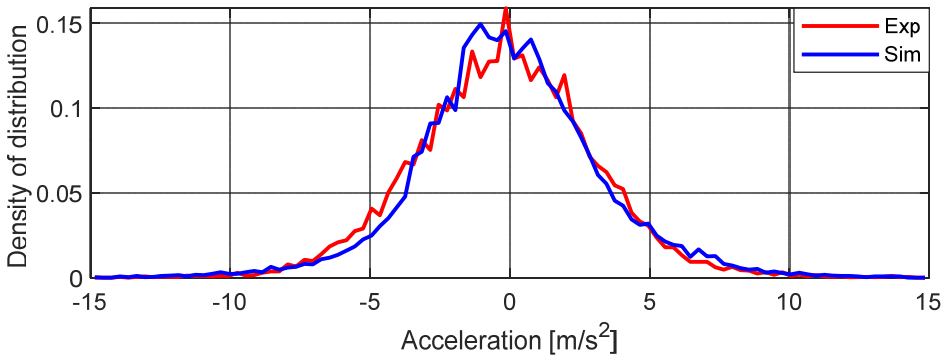

Figure 37. Density of probability distribution, acceleration on vehicle RA.

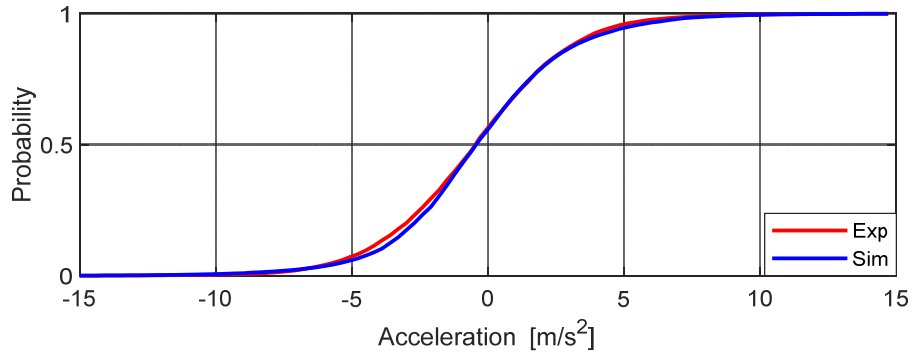

Figure 38. Distribution function, acceleration on vehicle RA.

The comparison of PDSs in the frequency range 0–10 Hz is shown in Figure 39.

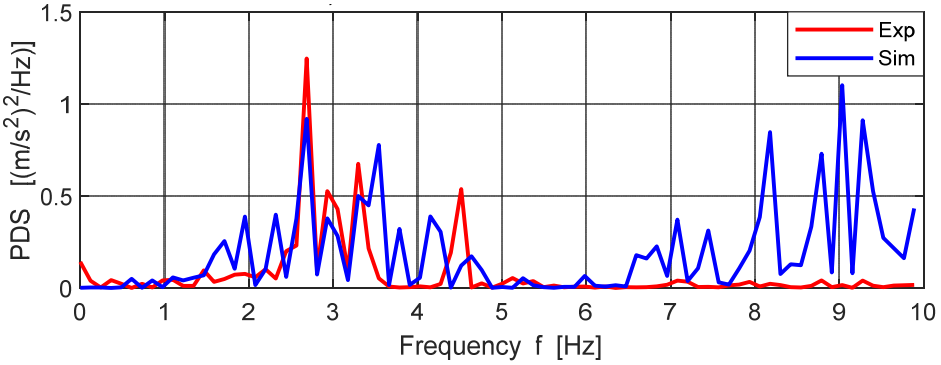

Figure 39. PSD of vertical accelerations on vehicle RA, 0–10 Hz.

7. Conclusions

The development of computers has created conditions for the development of simulation methods. Numerical simulation of vehicle movement along the transport structures is a real task today and can be done in real-time. This fact is confirmed by many articles dealing with this issue. Fewer articles are devoted to experimental measurements or comparisons between the results of numerical simulations and the results of experimental tests. The degree of accuracy of the various quantities obtained by numerical simulation is not the same. If differential equations are solved in the numerical simulation, where the sought functions have the meaning of deviations of certain points in time, then these quantities are calculated most accurately. The first derivatives of these functions according to time, the speed of movements, are already burdened with a larger error, and the second derivatives of these functions according to time, the acceleration of movements, are burdened with the largest error. On the contrary, when monitoring the response of a vehicle, measuring deviations is very problematic. Accelerations are measured most easily and accurately. Paradoxically, we are therefore forced to compare what we measure most accurately in the experiment with what we calculate the least accurately in the numerical simulation. When simulating the movement of a vehicle along the road, the unevenness of the road surface is a source of kinematic excitation of the vehicle, the contact between the wheel and the road is a point and changes discretely with the time step of the simulation. The source of the vehicle's kinematic excitation, in reality, is the movement of the wheel hub on the axle. This depends on the unevenness of the road, the unevenness of the tire, the pressure in the tire, and the size of the contact area between the tire and the road. The tire, therefore "smoothes out" the road profile. The real response is more settled than the response obtained by numerical simulation. It is generally accepted that road unevenness is governed by Gauss's law of distribution. If the unevenness is measured on a shorter section of the road, this may not always be evident, Figure 3. On the contrary, the response of the vehicle in all cases very well satisfies Gauss's law of distribution, Figure 40.

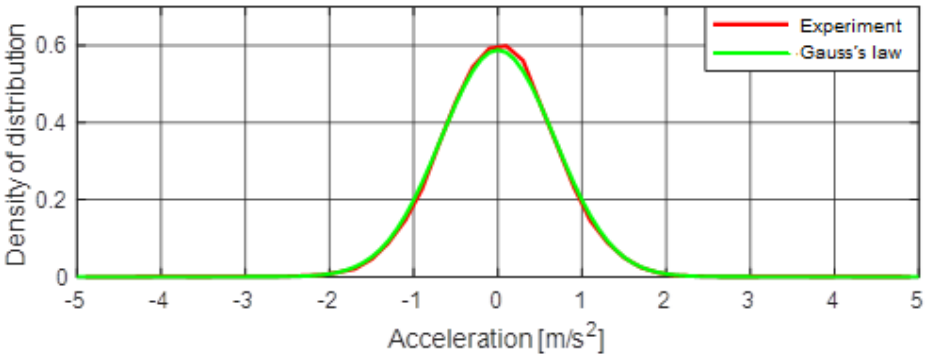

Figure 40. Density of probability distribution, acceleration on vehicle FA, V = 15.18 km/h.

All kinematic values of a vehicle's response depend on the speed of movement of the vehicle. Speed is the most important parameter entering into the vehicle–road interaction. It only makes sense to talk about the influence of all other parameters in connection with a certain specific speed of the vehicle. The theoretical curve (kinematic value versus vehicle speed) would have a large number of local maxima and spikes [13]. The position of the spikes is related to the discontinuous, step-changing course of the phase characteristics. The dependence of the root mean square (RMS) values for vertical accelerations in the center of gravity of the vehicle's sprung mass on the vehicle speed V used in the experiment is shown in Figure 41.

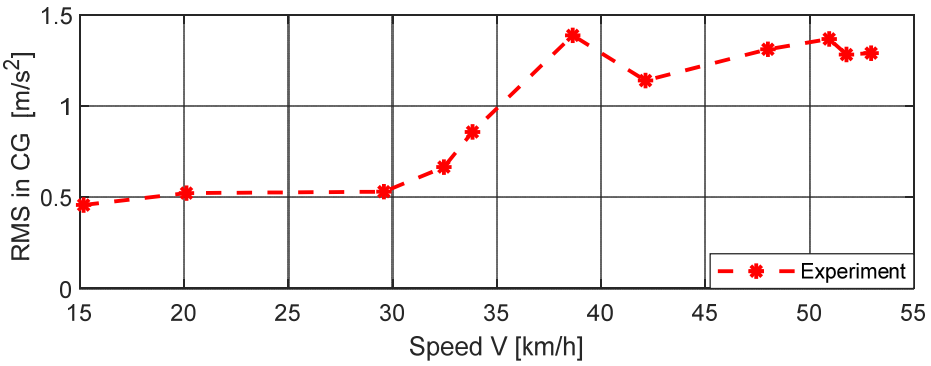

Figure 41. RMS of acceleration in vehicle CG versus speed V.

It does not make sense to compare the values of the two records at each point. It is more realistic to compare the basic statistical characteristics of both records. The comparison of basic statistical characteristics looks quite satisfactory for all monitored quantities. At low vehicle speeds, it was very good. With increasing speed, the rate of agreement decreased, but it could always be considered satisfactory.

The effective value RMS is considered in dynamics as a representative quantity of a given signal. Therefore, Table 8 compares the differences (simulation–experiment) expressed in percentage (experiment represents 100%) for the observed vehicle speeds and for the three characteristic points on the vehicle.

Table 8. Differences (Simulation–Experiment) of effective value RMS in (%).

	Difference (Simulation–Experiment) in (%) of Experiment		
Sensor	A1-CG	A2-FA	A3-RA
V = 15.18 km/h	−2.41%	+22.66%	+27.44%
V = 52.95 km/h	+0.55%	+2.22%	+0.46%

The biggest problem is with frequency spectra comparisons. Although the clusters of dominant frequencies in the experimental records and simulated records were similar, the powers were diametrically different. The largest disproportions related to the front axle response spectra.

Despite all the shortcomings we could mention, the methods of numerical simulation were applied in engineering practice. The advantage of numerical simulation is that it can perform interval analysis and simulate phenomena in the early stages of preparation of a structure, an analysis that could previously be obtained only experimentally on the finished structure itself; numerical simulation can also simulate phenomena that are problematic to model experimentally.

So far, an experiment is the only one way to verify the numerically obtained results. We do not consider one experiment to be sufficient. Due to the random nature of experimental measurements and the uniqueness of each passage of the vehicle on the pavement, we plan to perform another series of experimental measurements, which will provide a

more extensive dataset for verification of the results obtained. This will allow the field to move the state of knowledge another step forward.

Author Contributions: Conceptualization, J.M. and V.V.; methodology, J.M.; software, E.M.; validation, J.M., M.K., and E.M.; formal analysis, V.V.; investigation, J.M., M.K., and E.M.; resources, V.V.; data curation, J.M.; writing—original draft preparation, J.M., M.K., and E.M.; writing—review and editing, V.V.; visualization, V.V.; supervision, M.K.; project administration, J.M.; funding acquisition, J.M., M.K., V.V., and E.M. All authors have read and agreed to the published version of the manuscript.

Funding: This research was funded by a grant from the National Agency of the Slovak Republic VEGA, grant number 1/0006/20.

Institutional Review Board Statement: Not applicable.

Informed Consent Statement: Not applicable.

Acknowledgments: This paper was supported by a grant from the National Agency VEGA of the Slovak Republic, grant No. 1/0006/20.

Conflicts of Interest: The authors declare no conflicts of interest.

References

1. Stokes, G.G. Discussion of a Differential Equation relating to the Breaking of Railway Bridges. *Math. Phys. Pap.* **2010**, *8*, 178–220, doi:10.1017/cbo9780511702259.013.
2. Willis, R. *Appendix Report of the Commissioners Appointed to Inquire into the Application of Iron to Railway Structures*; Stationary Office: London, UK, 1849.
3. Wrigth, D.T.; Green, R. *Highway Bridge Vibration I: Review of Previous Studies*; Queen´s University Kingston: Ontario, UK, 1959.
4. Huang, T. *Vibration of bridges, Shock and Vibration Digest*; 1976; V. 8, N. 3, pp. 61-76, a Publication of the Shock and Vibration Information Center, Naval Research Laboratory, Washington, D.C., USA.
5. FrýbaL.; Steele, C.R. Vibration of Solids and Structures Under Moving Loads. *J. Appl. Mech.* **1976**, *43*, 524, doi:10.1115/1.3423922.
6. Frýba, L.; Maguire, J.R.; Wyatt, T.A.; Pritchard, B.; Fitzmauri, M.; Ricketts, N.; Mills, W.H. *Dynamics of Railway Bridges*; Thomas Telford Ltd.: London, UK, 1996.
7. Koloušek, V. *Dynamics in Engineering Structures*; Halsted Press: Sydney, NSW, Australia, 1973.
8. Melcer, J. *Dynamic Computation of Highway Bridges (in Slovak)*; University of Žilina: Žilina, Slovakia, 1997.
9. Melcer, J.; Lajčáková, G.; Martinická, I.; Králik, J. *Dynamics of Transport Structures (in Slovak)*; University of Zilina: Žilina, Slovakia 2016.
10. Melcer, J.; Lajčáková, G.; Valašková, V. *Moving Load Effect on Concrete Pavements*; Wydawnictwo Towarzystwa Slowaków w Polsce: Kraków, Poland, 2018.
11. Melcer, J.; Valašková, V. Vehicle model response in frequency domain. *MATEC Web Conf.* **2020**, *313*, 00009, doi:10.1051/matecconf/202031300009.
12. Cebon, D. *Handbook of Vehicle-Road Interaction*; Swets&Zeitlinger Publishers, Heereweg 347B2161 CA Lisse, The Netherlands, 1999.
13. Kulakowski, B.T.; Gardner, J.F. and Lowen, S.J. *Dynamic Modeling and Control of Engineering Systems*, 3rd ed.; Cambridge University Press: New York, NY, USA, 2009.
14. Rill, G. *Road Vehicle Dynamics, Fundamentals and Modeling*; CRC Press: Boca Raton, FL, USA, 2012.
15. MathWorks, Inc. *MATLAB 7.0.4 The Language of Technical Computing*, Version 7; MathWorks, Inc: Natick, MA, USA, 2005.
16. Valašková, V.; Vlček, J. Experimental Investigation of the Vehicle–Ground Interaction—Experiment Preparation and Preliminary Results. *Civ. Environ. Eng.* **2017**, *13*, 99–105, doi:10.1515/cee-2017-0013.
17. Park, D.-W.; Papagiannakis, A.T.; Kim, I.T. Analysis of dynamic vehicle loads using vehicle pavement interaction model. *KSCE J. Civ. Eng.* **2014**, *18*, 2085–2092, doi:10.1007/s12205-014-0602-3.
18. Martino, R. Modelling and Simulation of the Dynamic Behaviour of the Automobile. Ph.D. Thesis, Université de Haute Alsace, Mulhouse, France, 2005.
19. Quynh, L.V.; Hien, V.T.; Cong, N.T. Influence of Tire Parameters of a Semi-trailer Truck on Road Surface Friendliness. *Int. Res. J. Eng. Technol.* **2019**, *6*, 3674–3678.
20. Quynh, L.V.; Cuong, B.V.; Liem, N.V.; Long, L.X.; Truyen, V.T. Analysis of dynamic wheel loads of a semi-trailer truck with air.spring and leaf-spring suspension system. *ARPN J. Eng. Appl. Sci.* **2020**, *15*, 146–152.
21. Auersch, L. Theoretical and experimental excitation force spectra for railway-induced ground vibration: Vehicle–track–soil interaction, irregularities and soil measurements. *Veh. Syst. Dyn.* **2010**, *48*, 235–261, doi:10.1080/00423110802691515.
22. Pakrashi, V.; O'Connor, A.; Basu, B. A Bridge-Vehicle Interaction Based Experimental Investigation of Damage Evolution, Structural Health Monitoring. *Struct. Health Monit.* **2010**, *9*, 285–296.

23. Van Der Seijs, M.V.; De Klerk, D.; Rixen, D.J.; Rahimi, S. Validation of Current State Frequency Based Substructuring Technology for the Characterisation of Steering Gear–Vehicle Interaction. In *Topics in Experimental Dynamic Substructuring*; Springer: New York, NY, USA, 2013; Volume 2, pp. 253–266.
24. Levy, S.; Wilkinson, J.P.D. T*he Component Element Method in Dynamics with Application to Earthquake and vehicle Engineering*; McGraw-Jill: New York, NY, USA, 1976.
25. ISO. *ISO 8608 Mechanical Vibration, Road Surface Profiles, Reporting of Measured Data*; ISO: Geneva, Switzerland, 1995.